Int. J. Electrochem. Sci., 7 **(2012)** 5692 - 5707

International Journal of
ELECTROCHEMICAL
SCIENCE
www.electrochemsci.org

Studying and comparing the erosion-enhanced pitting corrosion of X52 and X100 steels

A. Rauf and E. Mahdi[*]

Qatar University, Department of Mechanical and Industrial Engineering, P.O.Box 2713, Doha, Qatar
[*]E-mail: elsadigms@qu.edu.qa

Received: 20 April 2012 / *Accepted:* 15 May 2012 / *Published:* 1 June 2012

The critical ratio of Cl^- to HCO^- concerning the corrosion rate has been determined with and without electrolyte erosion in 0.3 M $NaHCO_3$ by using various concentrations of NaCl for X52 and X100 steels. The open circuit potential (OPC) was recorded for both steels in electrolytes containing 0.3 M $NaHCO_3$ and 0.1 M NaCl without erosion, with electrolyte erosion, and with electrolyte-silica sand erosion. The electrochemical techniques like linear polarization resistance (LPR) and potentiodynamic polarization scans were used to study and compare the material resistance against synergistic impact of erosion and corrosion. Scanning electron microscope (SEM) and optical microscope were used to study the morphology of pitting corrosion in the absence and presence of erosion. The change in pitting potential due to electrolyte and electrolyte-silica sand impingement has been discussed. The microstructure and hardness of X52 and X100 steels were evaluated and discussed with respect to the erosion–corrosion behaviors. Cracks were observed at the inner wall of a pit because of silica sand impingement during erosion-enhanced pitting corrosion. X100 steel is more stable than X52 steel against pitting corrosion with and without erosion. X52 steel suffered pitting corrosion in standstill electrolyte containing chloride where as X100 not even in the presence of erosion. Pits propagate in the direction of erosion because of the impingement and disruption of the passive layer in that direction.

Keywords: OCP, erosion-corrosion, pitting, SEM

1. INTRODUCTION

Many materials used in chemical industries and other engineering applications confront erosion–corrosion [1] damages caused by impingement of solid particles. Electrochemical reactions deteriorate the material surface during corrosion where as the mechanical forces by solid particles during erosion. The sum of individual damages is less than the synergistic damage [2] caused by

corrosion and erosion. In an aqueous medium, the electrochemical reaction rate is low for passive material where as flowing streams with solid particles can damage the passive layer partly or fully [3,4] based on the impact angle, velocity, mechanical properties and shape of particles involved. The breakup of passive film causes the depassivation of the surface. Consequently the rate of electrochemical reactions increases due to repassivation as well as due to metallic dissolution [5,6]. The rate of passivation will be higher than the rate of metallic dissolution provided the metal potential is kept within the passivation range. Immediately after the impact and before the repassivation, the current transient peak is observed for a fraction of second. The level of this peak caused by erosion-enhanced corrosion depends on the scale of surface depassivation. Very short impact periods and highly localized deformations result in a very complicated impact phenomenon.

X52 and X100 are the low carbon steels having the carbon content of 0.15 % and 0.05 % by weight. The chemical composition of both steels by wt.% is shown in Table 1 in good comparison to other work [7]. The primary difference between X52 and X100 steels concerning alloying elements is the higher content of molybdenum, copper and nickel as well as the lower carbon content in case of X100 steel. Carbon steel pipes [8] are used universally for transporting crude oil and gas in bulky volumes over long distances. Bainitic ferrite exhibiting lath and granular type morphology [9] was discovered the major phase while martensite/austenite the second phase for X100 steel. H_2S and CO_2, if present in aqueous phases, can create very aggressive sour solution to damage the inner surfaces of pipeline material for its early failure. Uniform or localized corrosion including hydrogen induced damage creating blistering and cracking might be involved during material damage.

Corrosion study [10] indicates that savings can be made by using smaller wall thickness of high strength steels in long sections but the longterm corrosion of such steels must be addressed and managed. Operating at high pressure, the probability of internal corrosion for high strength pipelines increases because of the reduced strain hardening. Furthermore, high strength steels do not show plasticity in zones away from the groove and the risk per unit time increases for materials with high yield to ultimate tensile strength ratios. When the plasticity is locally limited to the corrosion groove then the burst pressure and reliability decrease. So re-qualification and optimal planning for inspection of the high strength steel is required.

Corrosion pattern can be uniform or localized depending on the constituents and conditions of the corrosive environment. J55 steel [11] may confront severe corrosion and protection problems because of Cl^- and HCO^- present in oil and gas fields. Zhang [11] observed that below the critical ratio for Cl^- to HCO^-, the corrosion rate of J55 increased with added NaCl, and conversely decreased above that level.

Table 1: Chemical composition of X52 and X100 steels by wt. %

Steel	C	Mn	Cr	Nb	Ni	Ti	V	Others
X52	0.13	1.09	0.017	0.035	0.013	0.005	0.036	Si=0.273, P=0.0176 S=0.012
X100	0.08	1.83	0.016	0.043	0.12	0.02	0.003	Mo=0.19, Cu=0.24 Carbon equivalent=0.46

To withstand high pressure and transmission rate for oil and gas transportation at long distance, the pipelines should be manufactured from high grade steel with high strength and excellent low temperature toughness. Therefore much research work about low carbon high strength steels is going on for testing mechanical and electrochemical properties as well as for developing new steels in place of currently used API X52 and X70 grade steels as pipeline materials.

2. EXPERIMENTAL

Cylindrical shaped metallic specimens were prepared from X52 and X100 steels to embed them individually in an epoxy with exposed surface area of 0.8 and 0.5 cm^2 with 1 cm (X52 steel) and 0.8 cm (X100 steel) corresponding diameters. Before starting the electrochemical measurements, the exposed surface of each metallic sample was ground with silicon carbide (SiC) paper up to 600 grit, washed with soapy water and ethanol (C_2H_5OH), and dried with the hot air stream.

The electrochemical cell fitted over a magnetic stirrer with three basic electrodes is used to perform both the simple and erosion induced corrosion measurements. The reference electrode used in the chloride containing electrolyte was a saturated calomel electrode (SCE) via a salt bridge with a luggin probe. The salt bridge avoids the contamination of electrolyte from the reference electrode and vice versa. The size of ceramic membrane used at the tip of luggin probe should be larger enough to provide conductive contact and smaller enough to avoid any solution contamination. The electrolyte solution was purged with nitrogen for 5 minutes before staring the test to remove any traces of oxygen. A gas dispenser was used for this purpose as shown in Figure 1.

Linear polarization resistance (LPR) measurements were carried out by polarizing the specimen from -10 mV to +10 mV versus open circuit potential at a scanning rate of 0.5 mV s^{-1}. The sample period of 0.2 s and repeat time of 2 min were used to measure the corrosion rate with the help of Gamry potentiostat. It was determined that how the corrosion rate increased with added NaCl below the critical ratio and decreased above that level by using liner polarization resistance (LPR) method. The behaviors of pitting corrosion were investigated with the help of different electrochemical techniques like potentiodynamic polarization curves and open circuit potential (OCP) measurements at different ratio of Cl^- to HCO^-. The potential sweep rate of 0.5 mV/s was used for scanning the polarization curves to obtain the passivation and pitting potential values with and without erosion. The changes in corrosion potential, pitting potential and pitting current were monitored in different corrosive environments for making comparisons among various corrosive and erosive-corrosive behaviors. For this purpose the corrosion was analyzed in different electrolytes (50:50) such as (a) 0.3 mol/l $NaHCO_3$; (b) 0.3mol/l $NaHCO_3$ + 0.1mol/lNaCl; (c) 0.3 mol/l $NaHCO_3$ + 0.2 mol/l NaCl; (d) 0.3 mol/l $NaHCO_3$ + 0.3 mol/l NaCl, (e) 0.3 mol/l $NaHCO_3$ + 0.4 mol/lNaCl and (f) 0.3 mol/l $NaHCO_3$ + 0.5 mol/l NaCl made from regent grade chemicals.

Magnetic stirrer with 350 revolutions per minute (rpm) stirring speed was used to create erosion in the electrolyte with and without 12 g of 75 µm silica sand. The OCP and potentiodynamic polarization scans were recorded for X52 and X100 steels. Scanning electron microscope (SEM) and

optical microscope were used to analyze the surface morphology after the erosion-induced corrosion tests.

In this work the mechanical properties of X52 and X100 steels were measured by conducting Rockwell indentation hardness tests. Hardness test was carried out on the piece cut in transverse direction from the steel bars of API X52 & X100 grades (Figure 1). Universal Hardness Tester of Indentec, UK (Model 8187.5 LKV) was used to determine Rockwell hardness according to ASTM E18 05.

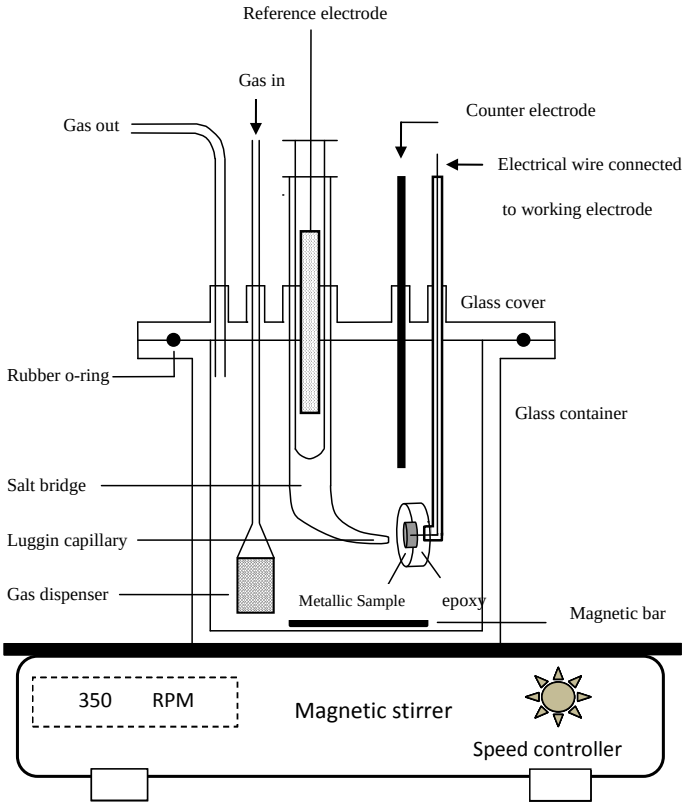

Figure 1: Electrochemical cell with three basic electrodes and stirring facility for performing simple corrosion and erosion-corrosion tests

3. RESULTS

3.1. Hardness and microstructure

The hardness of X100 steel was found to be higher than X52 steel as shown in Table 2. The microstructure of X52 steel shown in Figure 2 consists of alternate bands of pro-eutectoid ferrite and pearlite in a matrix predominantly of ferrite. The microstructure of X52 steel at higher magnification in which pearlite is completely resolved shows clearly alternate lamellae of ferrite and cementite. The microstructure of X100 steel shown in Figure 3 consists of bainitic ferrite having lath type (at few locations) and mostly granular morphology and martensite/austenite as the predominant phase. X100 steel is harder than X52 steel due to the presence of bainitic–ferrite in the microstructure along with

martensite/austenite as the second phase, as compared with the microstructure of X52 steel consisting of pro-eutectoid ferrite and pearlite in a matrix predominantly of ferrite.

Table 2: Hardness measured for X52 and X100 steels

Sr. No.	Material	Direction	Hardness					Average Hardness
1	X52	Surface to core	78.7	78.5	79.0	78.7	78.6	78.7 HRB
2	X100	Surface to core	24.9	25.6	25.7	25.6	26.0	25.6 HRC

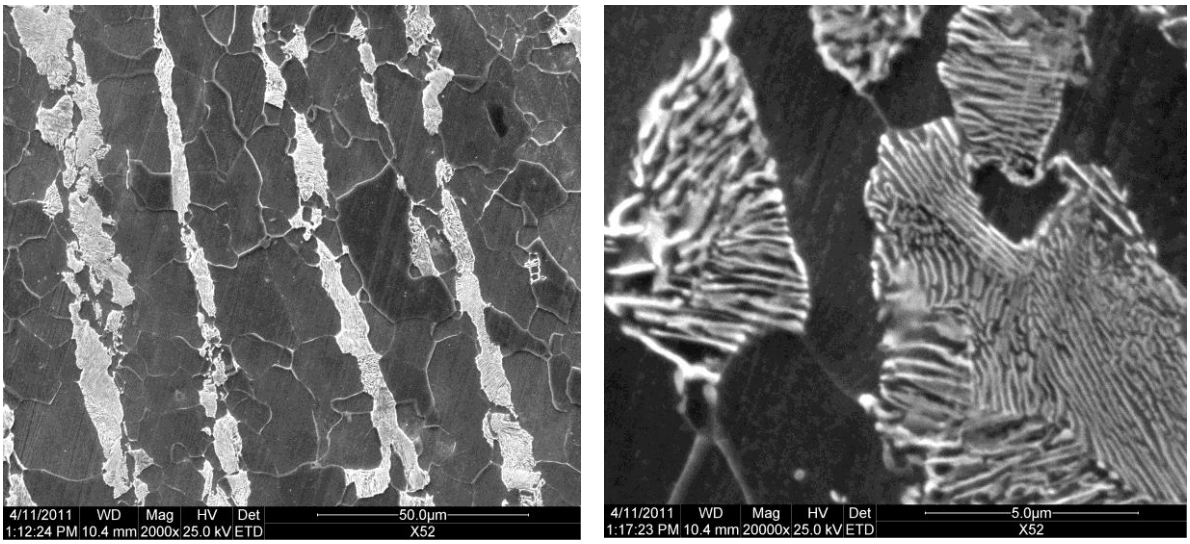

Figure 2. Microstructure of X52 steel at 2000X and 20000X magnifications

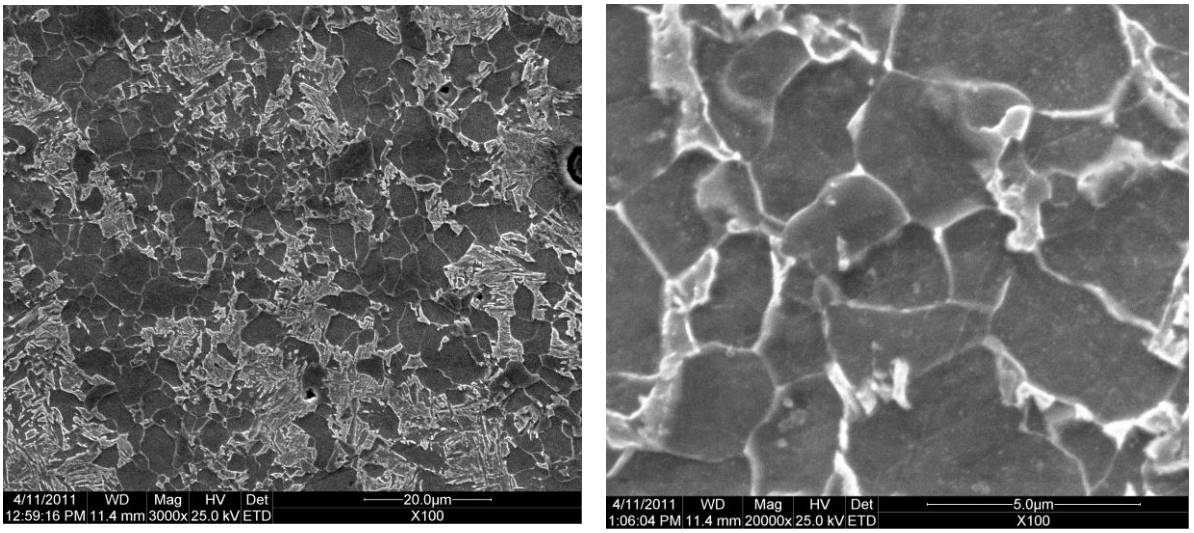

Figure 3. Microstructure of X100 steel at 3000X and 20000X magnifications

3.2. Critical ratio (Cl^- to HCO^-) for X52 steel

Below the critical ratio (1.66) for Cl^- to HCO^-, the corrosion rate increased with added NaCl, and conversely, decreased above that level for both steels (Figure 4 and Figure 6) without erosion.

3.2.1. Unstirred electrolyte

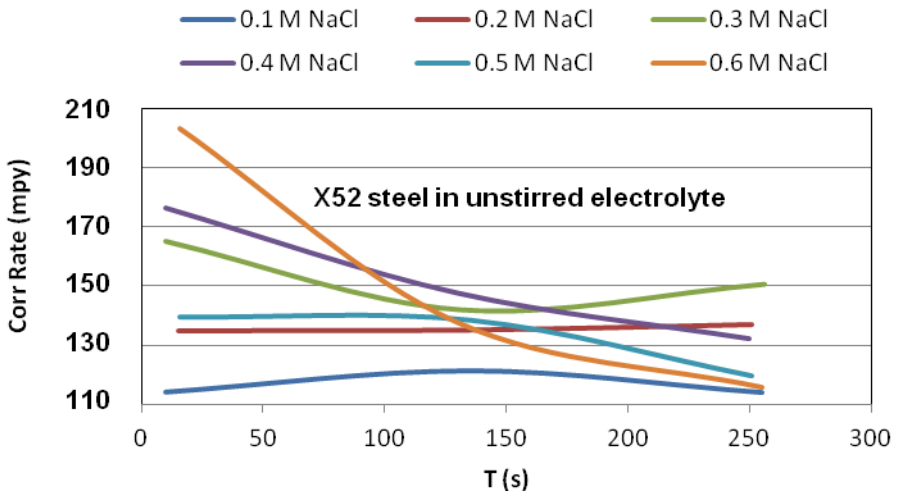

Figure 4. Corrosion rate measured for X52 steel in unstirred electrolyte with different chloride concentrations

3.2.2. Stirred electrolyte

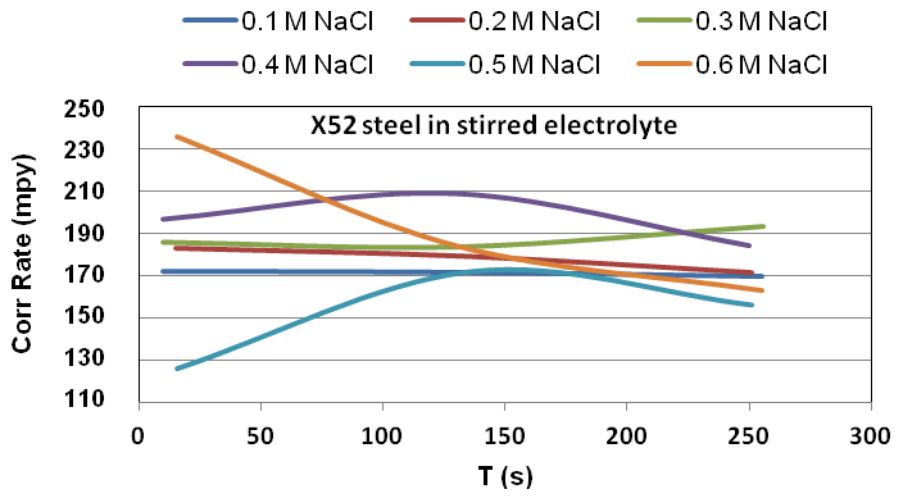

Figure 5. Corrosion rate measured for X52 steel with different chloride concentrations in stirred electrolyte

3.3. Critical ratio (Cl^- to HCO^-) for X100 steel

With erosion, below the critical ratio (1.33) for Cl^- to HCO^-, the corrosion rate increased with added NaCl, and conversely, decreased above that level for X100 steel as shown in Figure 7.

3.3.1. Unstirred electrolyte

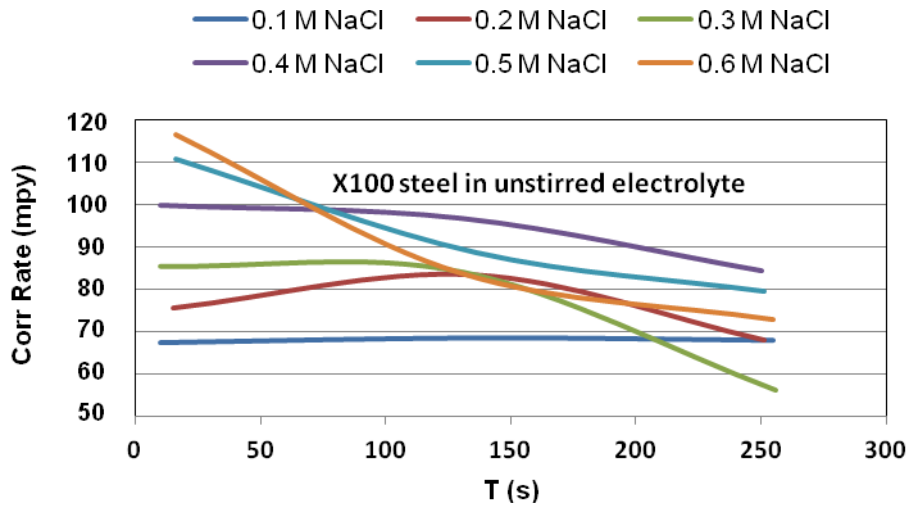

Figure 6. Corrosion rate measured for X100 steel with different chloride concentrations without fluid erosion

3.3.2. Stirred electrolyte

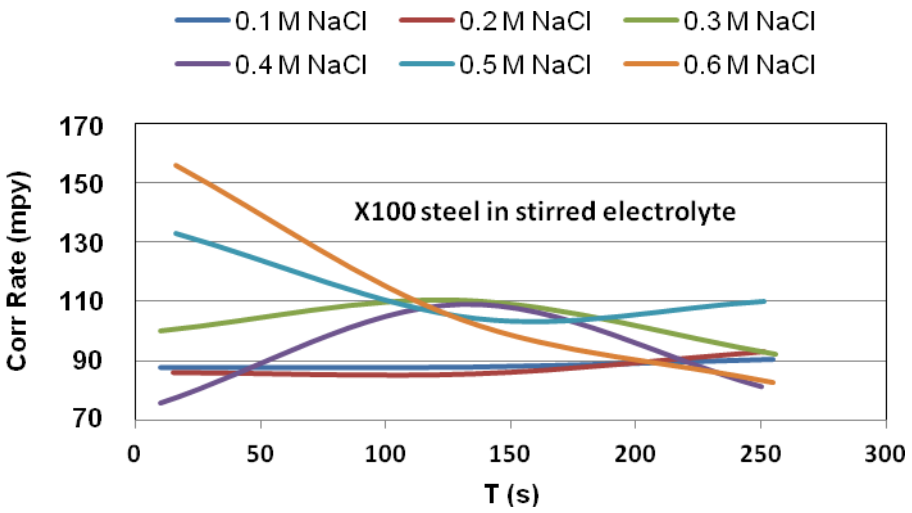

Figure 7. Corrosion rate measured for X100 steel with different chloride concentrations with fluid erosion

3.4. Open circuit potential (OCP)

3.4.1. OCP – without erosion

In unstirred electrolyte containing 0.3 M $NaHCO_3$ + 0.1 M NaCl (50:50) the OCP was recorded without erosion. After measuring the OCP for 20 h, circular pits were observed at the surface of X52 steel where as X100 steel exhibited good resistance against pitting corrosion.

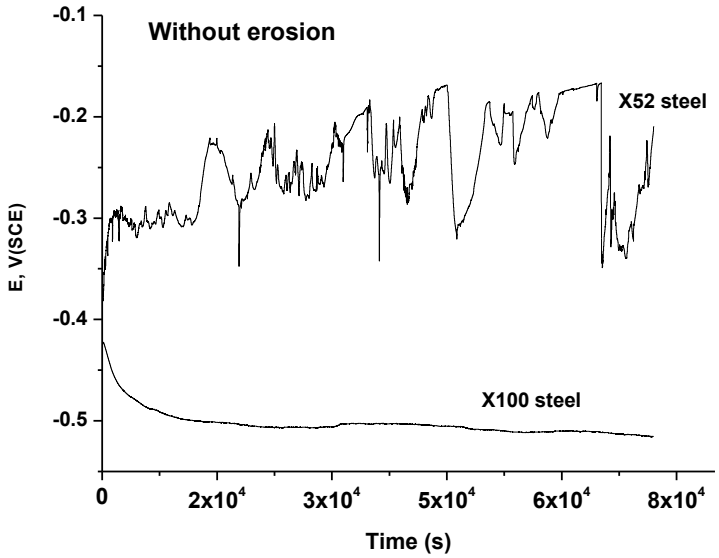

Figure 8. The OCP measured for X52 and X100 steels in unstirred electrolyte containing chloride

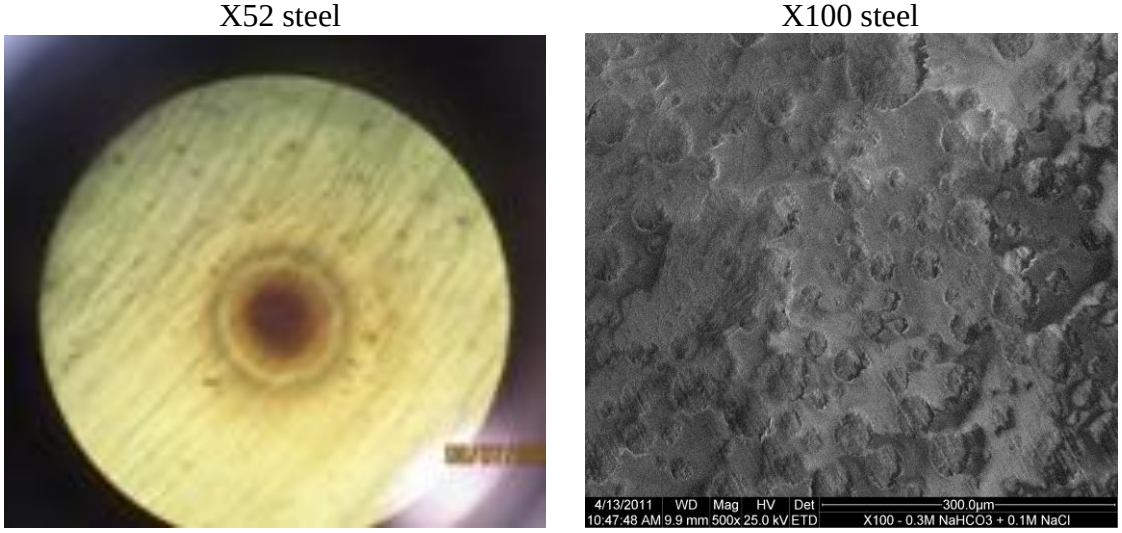

Figure 9. Circular pits observed after measuring OCP for X52 steel in unstirred electrolyte where as no pitting was observed for X100 steel in chloride containing sodium bicarbonate electrolyte.

3.4.2. OCP – with electrolyte erosion

Again pitting was observed only for X52 steel after 20 h experiment in which the OCP

fluctuated with many positive and negative peaks because of pitting corrosion. X100 steel suffered no pitting corrosion and hence the behavior of the OCP remained stable.

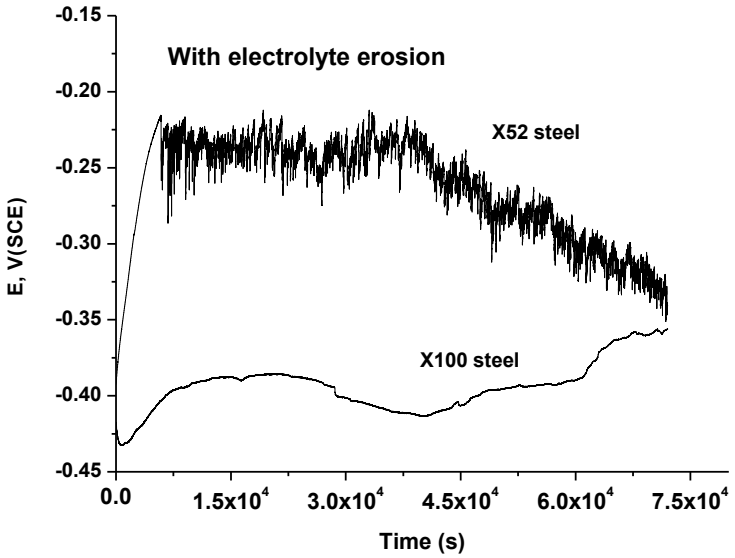

Figure 10. The OCP measured for X52 and X100 steels in electrolyte stirring at 350 rpm.

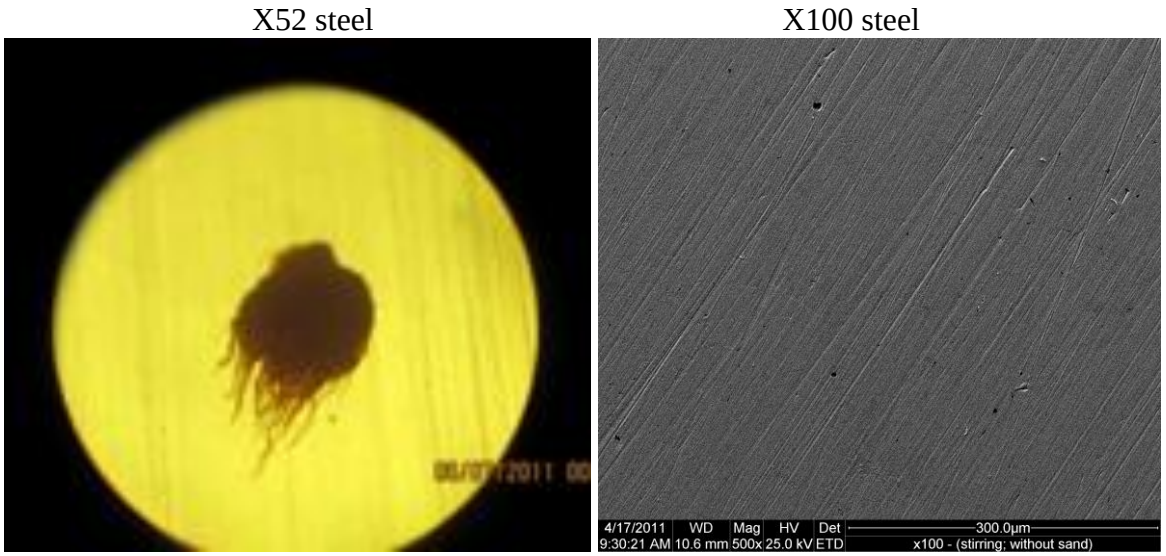

Figure 11. Pits were observed for X52 steel after measuring the OCP in stirred electrolyte. Pits tend to grow towards the direction of fluid impingement. X100 steel suffered no pitting corrosion unlike X52 steel after measuring the OCP in the presence of solution erosion at 350 rpm

3.4.3. OCP – with electrolyte and silica sand erosion

In stirred electrolyte containing silica sand, the behavior of the OCP (Figure 12) did not change significantly as with the case (Figure 10) of electrolyte erosion. X52 steel again suffered pitting

corrosion having special pattern along the direction of fluid impingement as shown in Figure 13. X100 steel suffered erosion marks due to the impingement of electrolyte-silica sand, but again resisted well against pitting corrosion as shown in Figure 13.

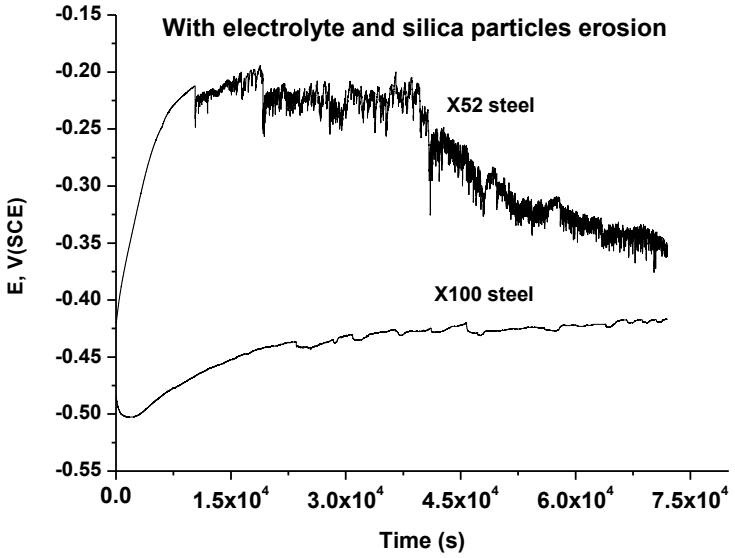

Figure 12. The OCP measured for X52 and X100 steels in electrolyte stirring at 350 rpm with silica sand.

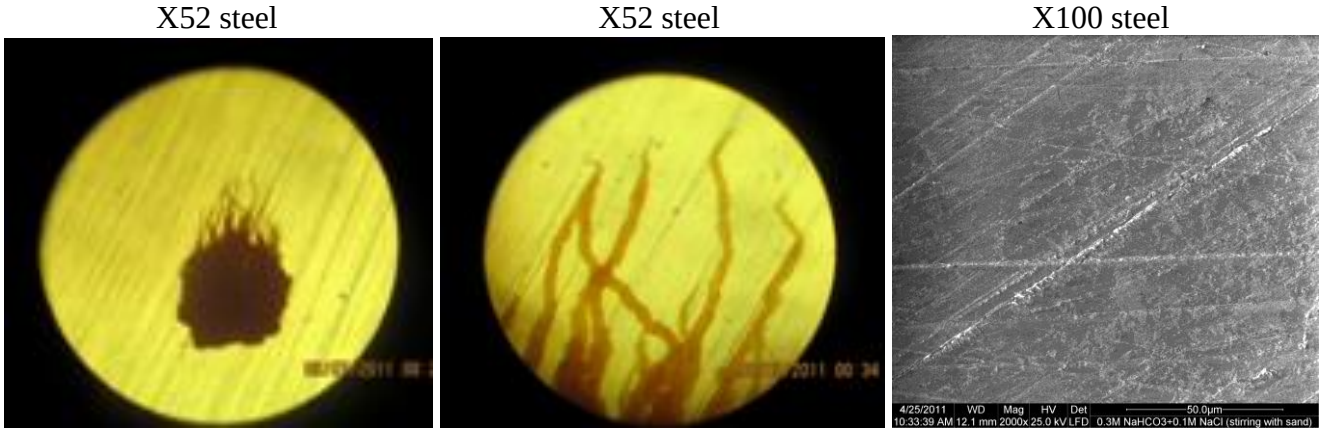

Figure 13. In electrolyte stirring at 350 rpm speed containing silica sand, X52 steel suffered pitting corrosion while X100 steel (right side) suffered erosion and uniform corrosion but no pitting corrosion.

3.5. Potentiodynamic polarization scans

3.5.1. Polarization scans – without erosion

During polarization scan in unstirred electrolyte, X52 steel yielded multiple corrosion potentials suggesting the instability of the passive layer at the sample surface. X52 steel is relatively more prone to localized corrosion due to the weaker or fragile surface passivation. Therefore X52 steel

demonstrates lower resistance against localized corrosion in chloride containing corrosive environment. On the other hand X100 steel shows better stability for the entire passivation region. Although no pitting was observed perhaps due to high concentration of bicarbonate (0.3 M) but transpassive potential was obtained. Alwaranbi [12] observed pitting corrosion for X100 steel only when the bicarbonate concentration was lower (0.01 M or 0.05 M) and no pitting when bicarbonate concentration was higher (0.1 M or 0.5 M).

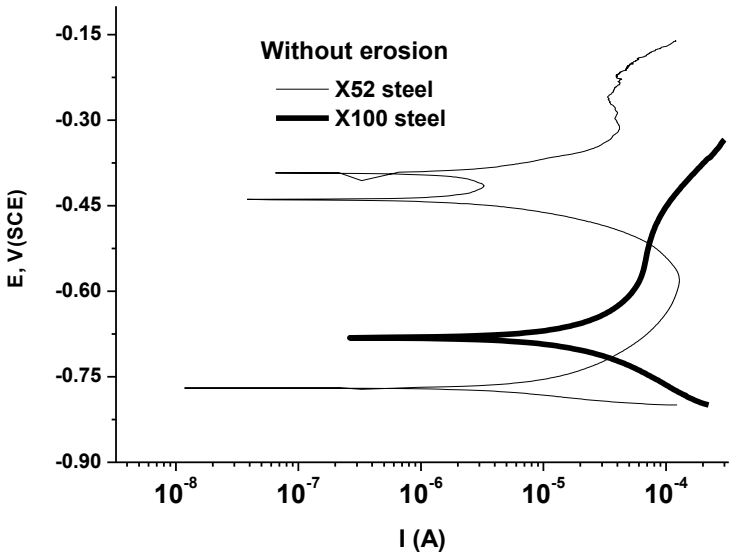

Figure 14. Potentiodynamic polarization scans for X52 and X100 steels in unstirred electrolytes.

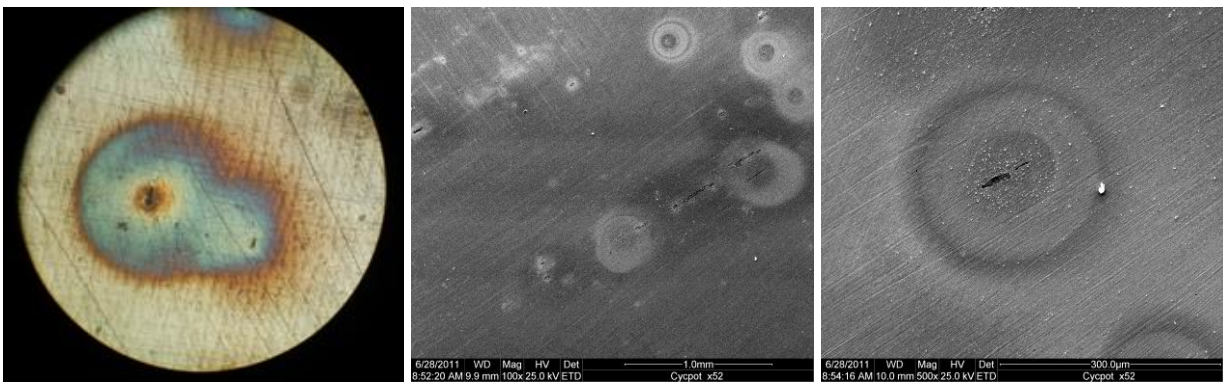

Figure 15. Pits were observed after polarization of X52 steel in unstirred solution.

3.5.2. Polarization scans – with electrolyte erosion

X52 steel suffered pitting corrosion in the presence of electrolyte erosion but X100 steel yielded multiple corrosion potentials showing instability of the passive layer although pitting was not observed.

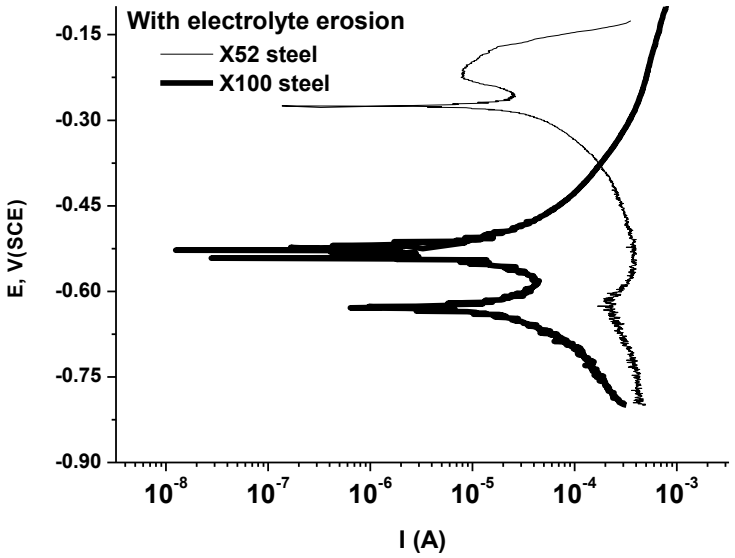

Figure 16. Potentiodynamic polarization scans for X52 and X100 steels in stirred electrolyte.

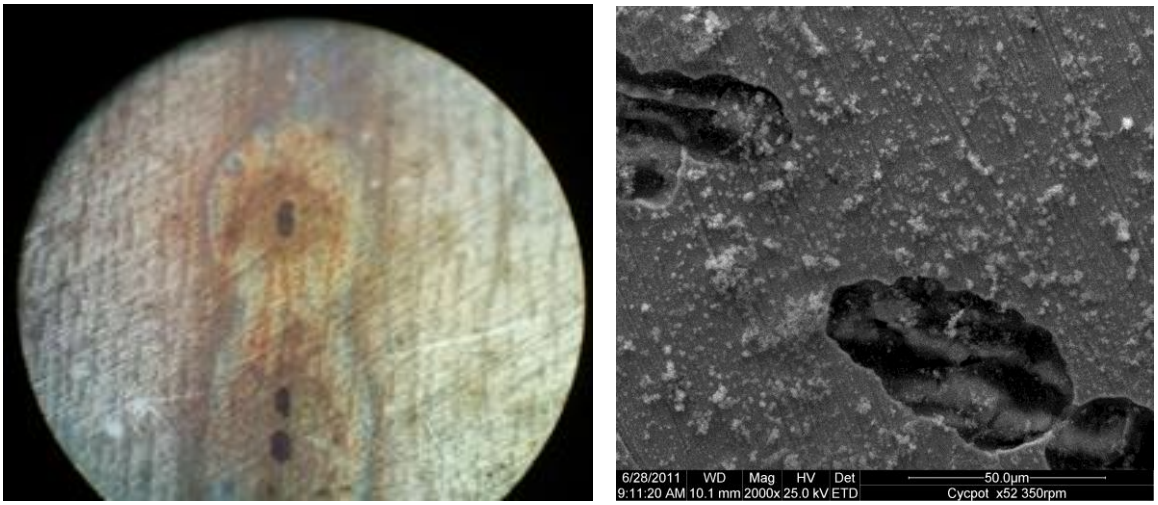

Figure 17. Pits were observed after polarization of X52 steel in stirred electrolyte

3.5.3. Polarization scans – with electrolyte and silica sand erosion

Due to the silica sand and electrolyte erosion, the shape of polarization curve remained same as that of electrolyte erosion, for X52 steel suffering pitting corrosion. The different incident was the occurrence of stress corrosion cracking inside the pit. This cracking was induced due to the impingement of silica sand at the inner surface of the pit. X100 steel did not again suffered pitting corrosion but the passivation region became smaller enabling the early reach of the transpassive potential in the presence of electrolyte-silica sand impingement.

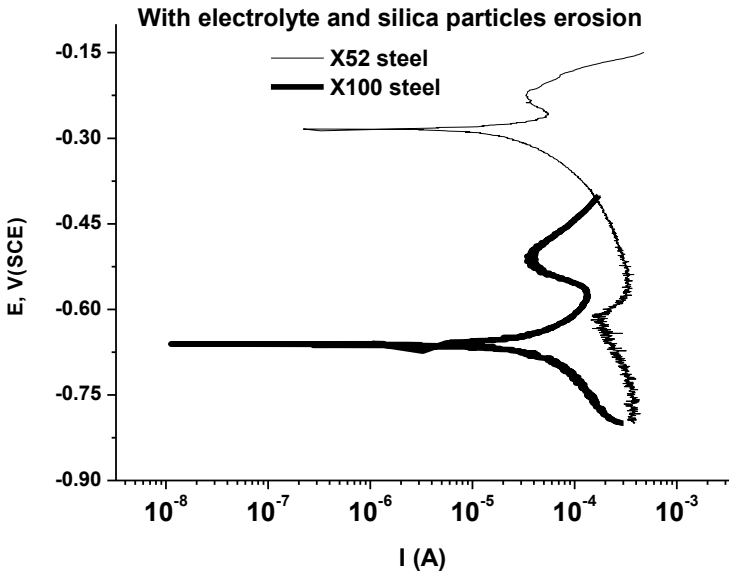

Figure 18. Potentiodynamic polarization scans for X52 and X100 steels in stirred electrolyte containing silica sand.

.

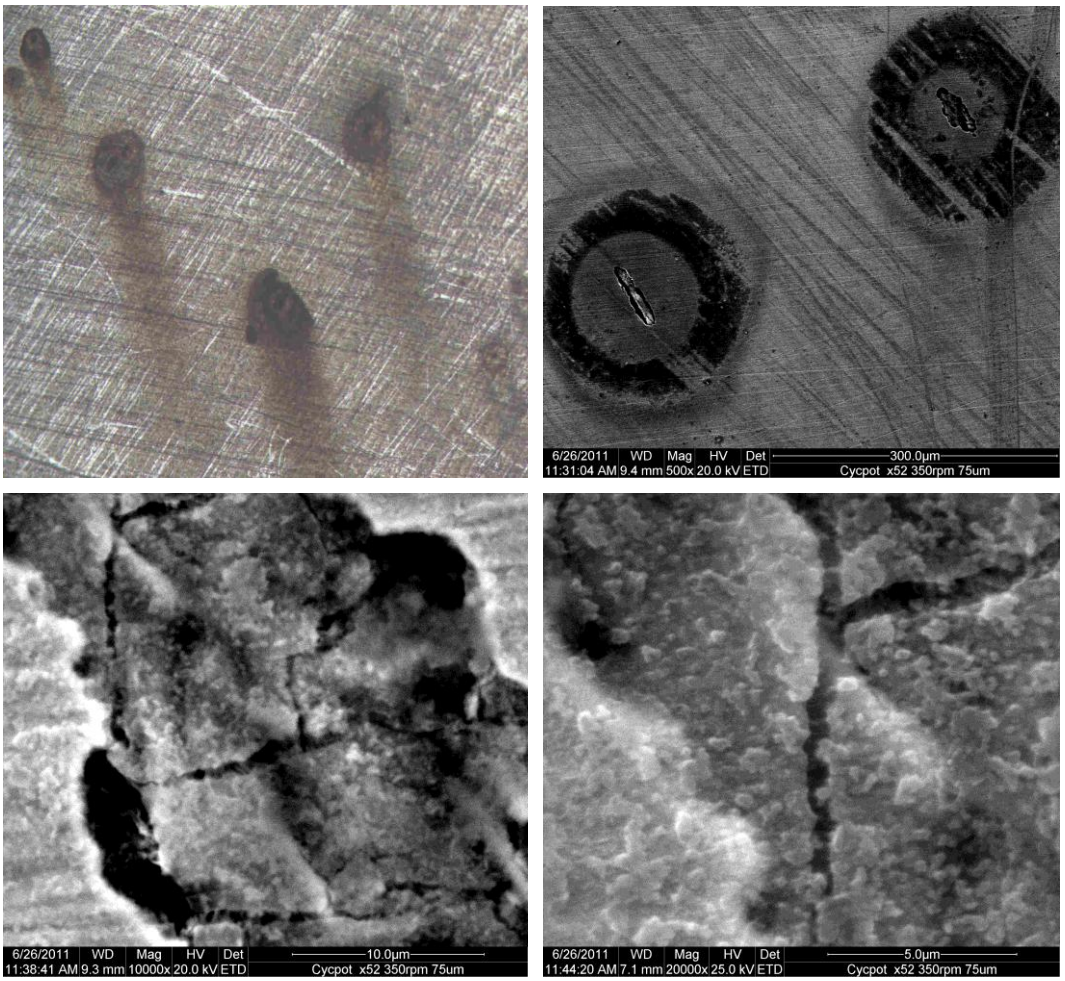

Figure 19.Pitting and stress corrosion cracking were observed for X52 steel after polarization scan accompanied by electrolyte-silica sand impingement.

4. DISCUSSION

The corrosion rate increased for both steels in stirred electrolyte as compared to unstirred electrolyte where as X52 steel corroded at a higher rate than X100 steel. The critical ratio for Cl^- to HCO^- regarding corrosion rate (Figures 4–7) remained same (1.66) for X52 and X100 steels in unstirred electrolytes where as decreased to 1.33 only for X100 steel in stirred electrolyte due to erosion-corrosion effect. In contrast to X52 steel, this decrease in the critical ratio for X100 steel is due to material behavior in the presence of erosion to achieve a critical point where further increase in NaCl concentration will result in the decreased corrosion rate. The stability of X100 steel to attain lower corrosion rate by gradual increase but relatively lower chloride content is facilitated by the stirred electrolyte. This is how the electrolyte erosion can control the corrosion mechanism. The metal passivation gradually decreases to facilitate enhanced corrosion rate due to gradual increase of NaCl but after complete breakdown of passive layer a critical point is reached where further increase in NaCl will result in sharp drop down of the corrosion rate. The number of active sites increases with added NaCl causing the acceleration of either uniform or pitting corrosion because of more Cl^- adsorbed at the material surface, until a critical point is reached [11].

The OCP fluctuates (Figure 8) continuously with many positive and negative peaks for X52 steel in the unstirred sodium bicarbonate solution containing chloride content. After 20 h of the test, many large pits (Figure 9) were observed visually at the sample surface of X52 steel. The fluctuations in the open circuit potential (OCP) are observed due to localized corrosion of stainless steels in the presence of chloride ions during pitting, stress corrosion cracking and crevice corrosion [13,14]. X100 steel, in contrast, suffers no pitting (Figure 9) and the OCP (Figure 8) remains noiseless. The potential slowly increases with mainly fluctuating peaks during pitting of X52 steel. With the increase in potential, pits can start and propagate [3] easily but repassivate in the metastable state and cease to grow if the potential is below the pitting potential.

In the stirred electrolyte, the OCP (Figure 10) for X52 steel gives noisier response with more number of fluctuating peaks suggesting rapid growth and propagation of the pits. With increased flow rate, the corrosion attach becomes stronger [15] where as the inhibiting efficiency decreases for Al–2.5 Mg alloy in 3 % NaCl. The induction time [3] is more to reach the stable pitting and the amplitude of the initial spikes is small due to metastable pitting in case of unstirred electrolyte as compared to the stirred electrolyte. Circular pits become elliptical (Figure 11) and tend to grow in the direction of electrolyte flow because of the removal of the passive layer due to erosive phenomena in that direction. The fall in the OCP is due to the stable pit growth [3] followed by the large fluctuations because of pitting propagation in a destructive way. The OCP continuously rises with some downwards peaks due to metastable pitting. The spikes in the potential can be regarded as the occurrence of metastable pits because they repassivate quickly, and the overall potential continues to rise [3]. The potential spikes are downwards towards more negative potential as the metastable pits activate but then repassivate and the potential returns to the rising baseline. X100 steel in the presence of stirring, gives a different response where the OCP (Figure 10) neither fluctuates nor decreases in the absence of pitting corrosion. During stable pitting, the potential fluctuation is observed both in positive and negative directions.

With the help of silica sand in stirred electrolyte an alike response of the OCP (Figure 12) is obtained well comparable without silica sand due to similar pitting behaviors for X52 steel. The breakdown of passive layer takes place in the direction of erosion causing the formation of elliptical pit mouth in the direction of erosion. X100 steel in the presence of stirred silica sand suffers mechanical erosion (Figure 13) but no pitting corrosion.

Severe pitting corrosion was observed in both cases after polarization scans (Figures 16 and 18) for X52 steel in the stirred electrolyte (Figure 17) as well as in the stirred electrolyte containing silica sand (Figure 19). For the cathodic polarization curves for X65 steel in solution containing NaCl and NaHCO3, limiting current density increases [16] and corrosion potential shifts positively by increasing electrode rotating speed facilitating the increased rate of the reduction reaction in the electrolyte. In contrast the anodic current density decreased with a similar trend of positive shift in the corrosion potential at high speed of electrode rotation. Due to electrolyte-silica sand impingement for X52 steel, the pitting potential shifted towards more negative value (-217 mV) as compared to the case (-208 mV) when only the electrolyte impingement was involved. In the same way the pitting current at pitting potential became higher (35 μA) in the presence of electrolyte-silica sand impingement in comparison to the case (8.2 μA) when electrolyte impingement was induced. The corrosion potential also shifted negatively (-283 mV vs. -275 mV) in the presence of electrolyte-silica sand erosion relative to the electrolyte impingement. After polarization scan during electrolyte-silica sand induced erosion for X52 steel, pitting corrosion was observed accompanied by the cracks (Figure 19) at the pit bottom due to the stresses applied by the electrolyte-silica sand impingement. Besides the pits having circular shape (Figure 19) at one side and elliptical on other side towards the direction of erosion, symmetric erosive lines at the steel surface were clearly found. The cracks (Figure 19) were observed at the inner wall of the pit through SEM analysis of the X52 steel surface.

In contrast, X100 steel exhibited good stability against localized corrosion after polarization scans (Figures 14, 16 and 18). Although transpassive potential was observed but no pitting corrosion during all three cases consisting of no erosion, electrolyte erosion and electrolyte-silica erosion (Figures 14, 16 and 18). A good passivation range (Figure 14) was observed for X100 steel without erosion but this range disappeared/narrowed (Figure 18) for the polarization scan during electrolyte-silica impingement. During electrolyte erosion, multiple corrosion potentials (Figure 16) were observed suggesting the instability of passive layer for X100 steel.

5. CONCLUSIONS

1. With erosion the critical ratio of Cl^- to HCO^- for X52 steel for the corrosion rate was found to be 1.66, where as this ratio decreased to 1.33 in case of X100 steel.
2. X100 steel is more stable against pitting than X52 steel without erosion, with electrolyte erosion and with electrolyte-silica erosion.
3. Pits tend to propagate in the direction of erosion.
4. The OCP increased until pitting potential is established
5. X52 steel suffered only pitting corrosion with electrolyte erosion, where as pitting and SCC with electrolyte-silica sand erosion.

ACKNOWLEDGEMENT
The authors are very grateful for the financial support from Qatar National Research Fund (QNRF) through National Priority Research Program (NPRP) No. 08-159-2-046.

References

1. F. Mohammadi, J. Luo, *Corros. Sci.* 52 (2010) 2994.
2. R.J.K. Wood, *Wear* 261, 1012 (2006).
3. K. Sasaki, G.T. Burstein, *Corros. Sci.* 49 (2007) 92.
4. A.J. Smitha, M. Stratmann, A.W. Hassel, *Electrochim. Acta* 51 (2006) 6521.
5. A.W. Hassel, A.J. Smith, *Corros. Sci.* 49 (2007) 231.
6. G.T. Burstein, K. Sasaki, *Electrochim. Acta* 46 (2001) 3675.
7. S. Dong-Han, K. Choong-Myeong, Y. Jang-Yong, K. Ki-Bong, Microstructure and Mechanical Properties of X80/X100 Grade Plates and Pipes, Proceedings of the Sixteenth (2007) *International Offshore and Polar Engineering Conference Lisbon*, Portugal, July 1-6, 2007.
8. R. Réquiz, S. Camero, A. L. Rivas, *Microsc Microanal* 11 (2005) 1992.
9. X. Tang, L.Y. Xu, Y.F. Cheng, *Corros. Sci.* 50 (2008) 1469.
10. M.A. Maes, M. Dann, M.M. Salama, *Reliab. Eng. Syst. Safe.* 93 (2008) 447–455.
11. J. Zhang and W. Zhao, *Surf. Interface Anal.* 43 (2011) 1018.
12. M.S. Alwaranbi (1999), Chloride pitting corrosion of API X-80 and X-100 high strength low alloy pipeline steels in bicarbonate solutions, *Master dissertation available online*, University of British Columbia, Canada.
13. K. Yamakawa, H. Inoue, *Corros. Sci.* 31 (1990) 503.
14. M. Hashimoto, S. Miyajima, T. Murata, *Corros. Sci.* 33 (1992) 885.
15. L. Vrsalović, M. Kliškić, J. Radošević, S. Gudić, *J. Appl. Electrochem.* 35 (2005) 1059.
16. G.A. Zhang, Y.F. Cheng, *Corros. Sci.* 51 (2009) 901.